Exploration of Double Perovskite Material Space via Machine Learning for Tandem Solar Cells

Z.Q. Wang[a], Z.H. Xiong[a], W.J. Hu[b], J.J. Jiang[a], Z.B. Cheng[a], Y.M. Xue[a], L. Peng[a,*] and J. Lin[a]

[a] *Department of Physics, Shanghai University of Electric Power, Shanghai 200090, China*
[b] *College of Electrical Engineering, Shanghai University of Electric Power, Shanghai 200090, China*

Received: 18.03.2025 & Accepted: 09.06.2025

Doi: 10.12693/APhysPolA.147.488 *e-mail: plpeng@shiep.edu.cn

The extensive compositional landscape of double perovskite materials ($A_2BB'X_6$) provides a promising basis for the design of tandem perovskite solar cells. However, the vast combinatorial space and multiple phase spaces also pose significant challenges in the engineering of efficient and stable tandem perovskite solar cells. In this work, machine learning is used to search for double perovskite materials suitable for tandem perovskite solar cells in a wide dataset containing over 1569248 hypothetical double perovskite materials. Finally, through first-principles calculations, it was found that double perovskite materials with two different space groups (i.e., $Fm\bar{3}m$-Rb_2BiAgI_6 and $I4/m$-$K_2CrErBr_6$) with stable and suitable bandgaps could serve as promising absorbers for tandem perovskite solar cells. Utilizing semiconductor device simulations, the tandem Rb_2BiAgI_6 solar cell and tandem $K_2CrErBr_6$ solar cell demonstrate power conversion efficiency of 24.00% and 42.78%, respectively. This research not only provides valuable insights into the compositional engineering of double-perovskite materials but also offers critical guidance for the development of high-efficiency tandem perovskite solar cells.

topics: tandem perovskite solar cells (TPSCs), double perovskite materials, machine learning, density functional theory

1. Introduction

Perovskite solar cells have achieved unprecedented progress, with certified efficiencies exceeding 26% in single-junction configurations [1, 2]. However, their practical performance remains bounded by the Shockley–Queisser limit ($\sim$ 33.7%), which fundamentally restricts the photon harvesting capacity of any single-bandgap absorber [3, 4]. In contrast, tandem perovskite solar cells (TPSCs) have demonstrated significant potential to surpass this limit by combining multiple materials, achieving power conversion efficiency (PCE) of up to 34.6% and approaching the theoretical efficiency limit of $\sim$ 43% for two-junction cells [5]. Perovskite materials, such as $MAPb(I_{1-x}Br_x)_3$, have shown great potential for TPSCs due to their tunable bandgaps and high absorption coefficients. However, they also bring a series of challenges, including the toxicity of Pb^{2+} ions and instability under operational stresses, which seriously hinder their large-scale commercialization [6].

Double perovskite (A2BB'X6) solves these two challenges through a vast combinatorial space and multiple phase spaces. Compared with common cubic perovskite materials, the preparation conditions for tetragonal perovskite materials are more relaxed. Additionally, due to their lower dissociation and formation energies, as well as lower phase transition temperature, they are relatively stable and possess considerable application potential [7]. For instance, researchers employed the γ-phase $CsPbI_3$ perovskite and successfully designed high-performance solar cells with an efficiency of up to 21.15% and high stability by introducing carbonyl and thiophene groups as passivators in the acyloin ligand (1,2-di(thiophen-2-yl)ethane-1,2-dione (DED)) [8]. Double perovskite materials present an immense opportunity for identifying suitable tandem top-cell materials. However, experimental synthesis struggles with the rapid bandgap characterization, and density functional theory (DFT) becomes computationally prohibitive at this scale [9, 10]. How to quickly filter out materials that meet specific characteristics from a massive number of candidates in a limited time has become a key issue in current research.

With the rapid advancement of artificial intelligence, machine learning has emerged as a crucial tool for large-scale screening and optimized design of new materials. For example, researchers

established a database encompassing decomposition energies through high-throughput DFT calculations and trained a machine learning model to analyze the formability of diverse perovskites [11]. A novel machine learning framework that integrates material-related knowledge into the data preprocessing stage was proposed, effectively enhancing the accuracy of predicting formation enthalpies and bandgaps of materials [12]. A recent study predicted the bandgaps of 23314 unexplored double perovskites in the periodic table and identified six new double perovskites with appropriate bandgaps [13]. These advancements highlight the transformative potential of machine learning in accelerating the discovery and optimization of perovskite materials.

In this research, we use machine learning to investigate double perovskites with two space groups ($Fm\bar{3}m$ and $I4/m$), aiming to identify promising candidates for TPSCs. Firstly, we generated a database of 1569248 double perovskite candidates. Subsequently, a dataset comprising 2400 materials using DFT calculations was constructed, which served as the foundation for training machine learning models to analyze and predict the properties of double perovskite materials. After screening, we identified 45 perovskite materials that exhibit thermodynamic stability and suitable bandgaps. Ultimately, two double perovskite materials were validated through first-principles calculations and can serve as absorbers in TPSCs. The simulation using COMSOL Multiphysics confirmed their potential for device applications.

2. Method

2.1. Structural stability

Goldschmidt [14] proposed the concept of tolerance factor T_f to evaluate the stability of perovskite-type structures. It is defined as

$$T_f = \frac{R_\mathrm{A} + R_\mathrm{B}}{\sqrt{2}\,(R_\mathrm{B} + R_\mathrm{X})}, \tag{1}$$

where R_A represents the ionic radius of the element at the A-site, R_B represents the ionic radius of the element at the B-site, and R_X represents the ionic radius of the element at the X-site. To guarantee the stability of the crystal structure, we control the tolerance factor T_f of the perovskite within the range of 0.8 to 1.2, which, to a certain extent, ensures the feasibility of the structure formation [15].

To describe the spatial adaptability of ions in the octahedral position within the crystal [16], we use the octahedral factor $O_f = \mu$. It is defined as

$$O_f = \frac{R_\mathrm{X}}{R_\mathrm{B}}. \tag{2}$$

We selected the O_f range to be between 0.4 and 0.8 [17]. Within this range, the X-site and B-site elements are expected to form a stable octahedral structure. The corresponding data of the ionic radii of the elements are taken from the literature [18].

2.2. DFT calculations

In this work, all DFT computations were conducted within the Vienna *Ab initio* Simulation Package (VASP) [19–21]. We utilized the Perdew–Burke–Ernzerhof (PBE) form of the exchange–correlation functional and the projector augmented wave (PAW) approach, along with a plane-wave basis set with an energy cutoff of 500 eV for structural optimization and static calculations. The integration of the Brillouin zone was accomplished using a $4 \times 4 \times 4$ Γ-centered k-point grid scheme. During the process of structural optimization, we employed the conjugate gradient algorithm to optimize the atomic positions, with the electronic step convergence criterion set to 3×10^{-4} eV and the ionic relaxation convergence criterion to 3×10^{-5} eV/Å. To enhance the accuracy of bandgap calculations, we adopted the hybrid generalized HSE06 method; this allowed us to improve the prediction of semiconductor bandgaps [22]. To verify the thermal stability of the materials, we performed *ab initio* molecular dynamics (AIMD) simulations [23, 24], simulating the evolution of the crystal at 500 K. We utilized a $2 \times 2 \times 2$ supercell, with the AIMD simulation time step being 1 fs and the total simulation duration being 5 ps.

2.3. Optical properties

The complex refractive index $n'(\omega)$ of a given material constitutes a significant physical quantity for delineating the optical properties of the material. It is composed of a real part and an imaginary part [25]

$$n'(\omega) = n(\omega) + \mathrm{i}k(\omega), \tag{3}$$

where the real part $n(\omega)$ and the imaginary part $k(\omega)$ can be represented, respectively, as

$$n(\omega) = \left(\frac{\sqrt{\varepsilon_1^2 + \varepsilon_2^2} + \varepsilon_1}{2}\right)^{1/2} \tag{4}$$

and

$$k(\omega) = \left(\frac{\sqrt{\varepsilon_1^2 + \varepsilon_2^2} - \varepsilon_1}{2}\right)^{1/2}. \tag{5}$$

Herein, $\varepsilon_1(\omega)$ and $\varepsilon_2(\omega)$ originate from the real and imaginary parts of the dielectric function $\varepsilon(\omega)$

$$\varepsilon(\omega) = \varepsilon_1(\omega_1) + \mathrm{i}\varepsilon_2(\omega_2). \tag{6}$$

The real and imaginary parts of this complex function are, respectively,

$$\varepsilon_1(\omega) = 1 + \frac{2P}{\pi}\int_0^\infty \mathrm{d}\omega' \, \frac{\varepsilon_2(\omega')\,\omega'}{\omega'^2 - \omega^2 + \mathrm{i}\eta} \tag{7}$$

and

$$\varepsilon_2(\omega) = \frac{4\pi^2 e^2}{\Omega} \times \lim_{q\to 0} \frac{1}{|\boldsymbol{q}|^2} \sum_{c,v,\boldsymbol{k}} 2\omega_{\boldsymbol{k}}\, \delta(E_c + E_v - \omega)\, \left|\langle c|\boldsymbol{e}\cdot\boldsymbol{q}|v\rangle\right|^2, \tag{8}$$

where P denotes the principal value, η is the complex shift parameter, $\langle c|\boldsymbol{e}\cdot\boldsymbol{q}|v\rangle$ is the integrated optical transitions from the valence states (v) to the conduction states (c), $\boldsymbol{e}$ is the polarization direction of the photon, and $\boldsymbol{q}$ is the electron momentum operator.

2.4. Semiconductor properties

The effective density of states N_c/N_v can be expressed with the use of the following formulae

$$N_c = 2\Big(\frac{m^*_{dn}\, k_{\mathrm{B}} T}{2\pi\hbar^2}\Big)^{3/2}, \tag{9}$$

$$N_v = 2\Big(\frac{m^*_{dp}\, k_{\mathrm{B}} T}{2\pi\hbar^2}\Big)^{3/2}, \tag{10}$$

where m^*_{dn} is the effective mass of the state density of the bottom electron in the conduction band, m^*_{dp} is the effective mass of the state density of the top hole in the valence band, k_{B} is the Boltzmann constant (1.380649×10^{-23} J/K), and T is the absolute temperature in Kelvin. The quantities m^*_{dn} and m^*_{dp} can be further calculated using the following formulae

$$m^*_{dn} = s^{2/3}\big(m_l\, m_t^2\big)^{1/3}, \tag{11}$$

$$m^*_{dp} = \Big[(m_p)_l^{3/2} + (m_p)_h^{3/2}\Big]^{2/3}, \tag{12}$$

where s is the number of symmetric states at the bottom of the conduction band, m_t is the effective mass of electrons in the transverse direction (i.e., x and y direction), m_l is the effective mass of electrons in the longitudinal direction (i.e., z direction), $(m_p)_l$ is the effective mass for light holes, $(m_p)_h$ is the effective mass for heavy holes. According to the formula for effective mass

$$\frac{1}{m^*} = \frac{1}{\hbar^2}\frac{\partial^2 E(k)}{\partial k^2}. \tag{13}$$

The effective mass in different directions can be calculated using the first-principles to compute the energy bands of materials.

2.5. Device simulation

In this paper, the device is simulated using the Semiconductor Module and the Wave Optics Module within the COMSOL Multiphysics package. The internal quantum efficiency (IQE) is calculated in the Semiconductor Module by modeling the carrier transport and recombination processes. Concurrently, the light extraction efficiency (LEE) is computed in the Wave Optics Module by simulating the propagation and outcoupling of the generated light. The external quantum efficiency (EQE) of the device is then determined as the product of IQE and LEE (EQE = IQE × LEE). The computation methodology involving optical and electrical equations is as follows. First, Maxwell's equation

$$\nabla\times(\nabla\times\boldsymbol{E}) - k_{\mathrm{B}}^2\varepsilon_r\boldsymbol{E} = 0 \tag{14}$$

is solved to obtain detailed spatial distributions of electrical and magnetic fields to evaluate optical absorption. In (14), $\boldsymbol{E}$ is the electric field, $\boldsymbol{k}_0$ is the wave-vector of incident light, and ε_r is the relative permittivity. The photo-generation rate can be calculated by

$$G_{\mathrm{photo}}(\lambda) = \frac{\varepsilon''\,|\boldsymbol{E}|}{2h}, \tag{15}$$

where h is Planck's constant and ε'' is the imaginary part of ε_r, which is a function of wavelength given by the equation $\varepsilon_r(\lambda) = (n(\lambda) - \mathrm{i}k(\lambda))^2$. Therefore, the total photo-generation rate (G_{tot}) is calculated by integrating $G_{\mathrm{photo}}(\lambda)$ over the given wavelength range from 300 to 1200 nm; this is shown as $G_{tot}(\lambda) = \int_{\lambda_{\min}}^{\lambda_{\max}} \mathrm{d}\lambda\; G_{\mathrm{photo}}(\lambda)$.

Further, the Poisson and continuity equations, respectively,

$$\nabla\cdot(\varepsilon_0\varepsilon_r\nabla\phi) = -\rho, \tag{16}$$

and

$$\frac{\partial n}{\partial t} = \frac{1}{q} = \nabla\cdot\boldsymbol{j}_n - U_n + G_n, \tag{17}$$

$$\frac{\partial p}{\partial t} = \frac{1}{q} = \nabla\cdot\boldsymbol{j}_p - U_p + G_p, \tag{18}$$

are solved in the simulation to evaluate the current density–voltage (J–V) characteristics of solar cells. In (16)–(18), $\nabla\phi$ is the electrostatic potential, ρ is the charge density, q is the electron charge, ε_0 is the vacuum permittivity, and both G_n and G_p are the total photo-generation rates in the optical simulation ($G_n = G_p = G_{tot}$). In the continuity equations, the terms U_n and U_p denote the net recombination rates for electrons and holes, respectively. The definition of charge density can be written as

$$\rho = q\,(n - p + N_A - N_D), \tag{19}$$

where n and p are the electron and hole concentrations, respectively; N_A and N_D are the acceptor and donor density, respectively; $\boldsymbol{j}_n$ and $\boldsymbol{j}_p$ are the current densities of electron and hole, respectively. These quantities are described by the electron and hole drift–diffusion process as follows

$$\boldsymbol{j}_n = -q\,\mu_n\, n\nabla\phi + q\,D_n\nabla n, \tag{20}$$

$$\boldsymbol{j}_p = -q\,\mu_p n\,\nabla\phi + q\,D_p\nabla p, \tag{21}$$

where μ_n and μ_p represent the electron and hole mobility, respectively, and D_n and D_p are the electron and hole diffusion coefficients, respectively.

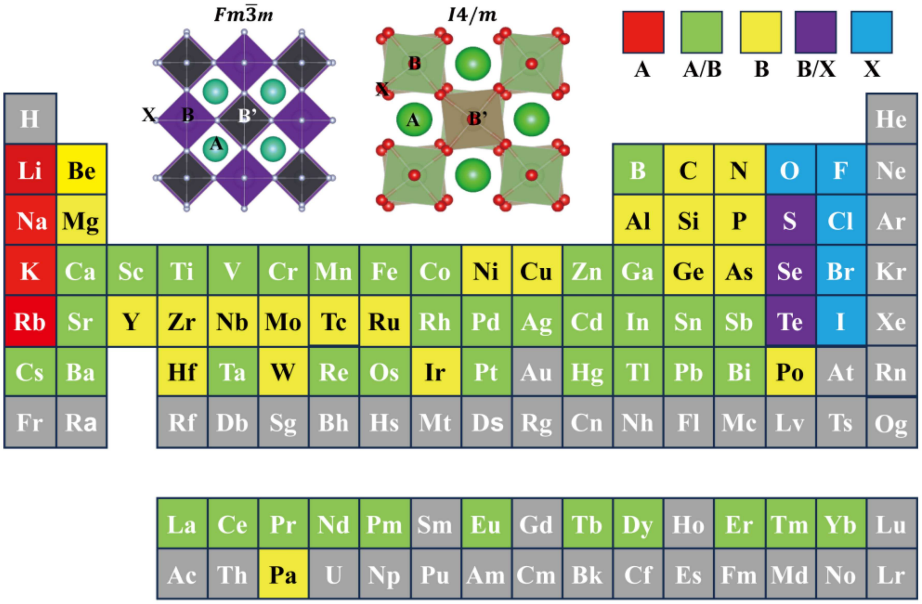

Fig. 1. Schematic crystal structure of $A_2BB'X_6$-type double perovskite material ($Fm\bar{3}m$ and $I4/m$) and chemical elements used in the design of each site. The red color indicates the element chosen for the A-site. Green indicates the element chosen for both the A-site and B/B'-site. Yellow indicates the element chosen for the B/B'-site. Purple indicates the element chosen for both the B-site and X-site. Blue indicates the element chosen for the X-site.

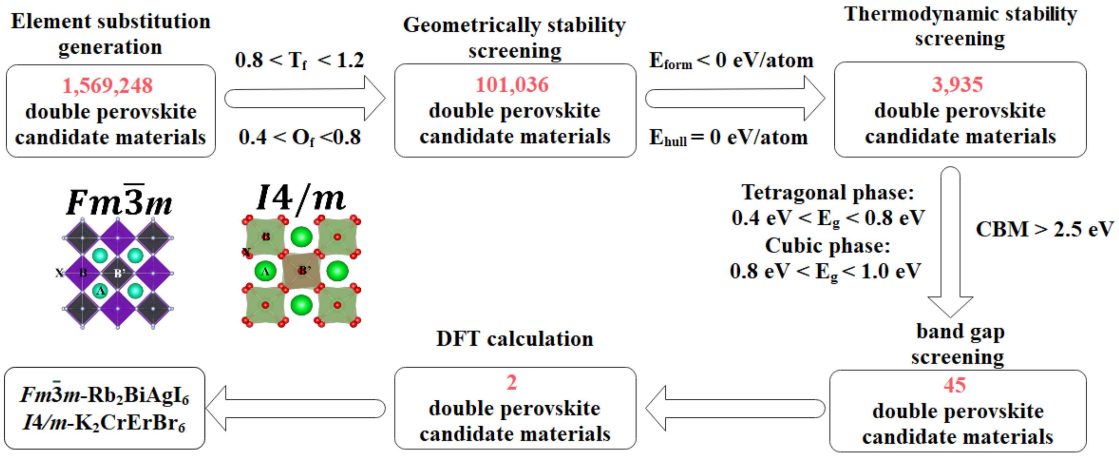

Fig. 2. Screening flowchart. The screening process and standards of double perovskite materials.

Moreover, Shockley–Read–Hall (SRH) recombination is considered a recombination model in our simulations, because it has been proven to be the dominant recombination mechanism in perovskite solar cells (PSCs). In turn, the interfaces are treated as an ideal ohmic contact in our simulations. SRH recombination is calculated as follows

$$R_{\mathrm{SRH}} = \frac{n\,p - n_i^2}{\tau_p\,(n + n_1) + \tau_n\,(p + p_1)}, \tag{22}$$

where n_i is the intrinsic carrier concentration, τ_p and τ_n represent the hole and electron SRH lifetimes, respectively, p_1 is the hole trap level density, and n_1 is the electron trap level density expressed.

3. Results and discussion

To systematically identify $A_2BB'X_6$-type double perovskite materials suitable for TPSCs, we have considered all potential elements in double perovskite, as illustrated in Fig. 1. In this process, we strictly adhered to the principle of valence conservation. Specifically, we selected 44 elements for the A-site, 65 elements for the B/B'-site, and 8 elements from groups V and VI for the X-site. By employing this combined approach, we generated 1569248 candidate double perovskite materials for each of the two distinct space groups.

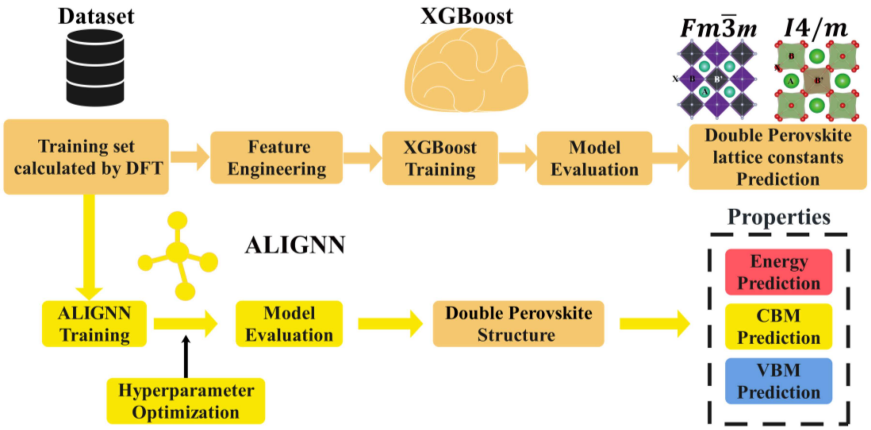

Fig. 3. Machine learning framework. The eXtreme Gradient Boosting (XGBoost) [26] model is primarily employed for predicting the lattice constants of double perovskite materials, and the Atomistic Line Graph Neural Network (ALIGNN [27] model further uses this information of lattice constants to predict various properties of the double perovskite materials.

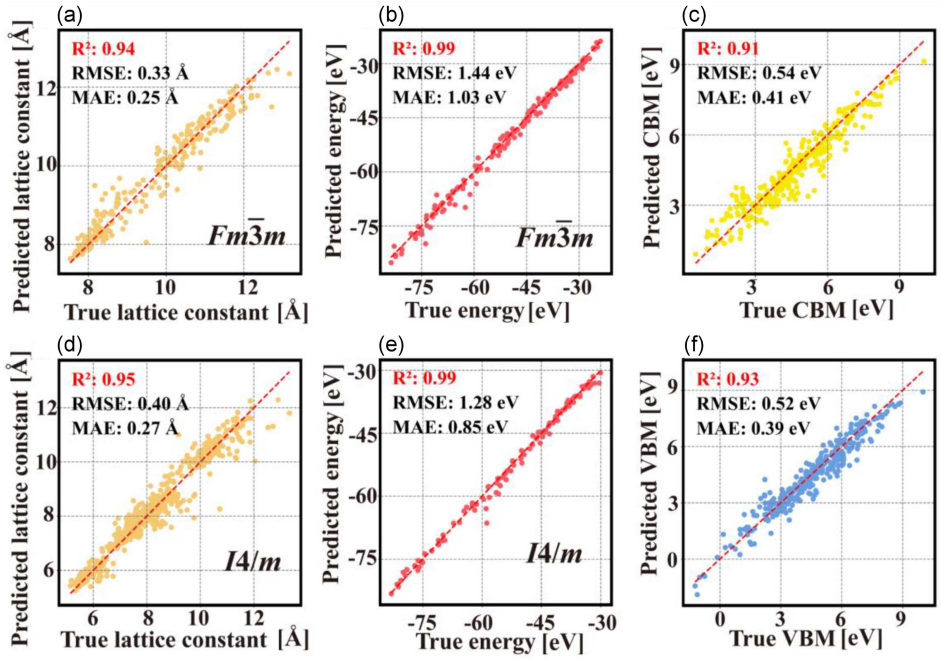

Fig. 4. Prediction performance of machine learning models. (a) Prediction of the lattice constant of the cubic phase by the XGBoost model. (b) Prediction of the lattice constant of the tetragonal phase by the XGBoost model. (c) Prediction of the total energy of the cubic phase by the ALIGNN model. (d) Prediction of the total energy of the tetragonal phase by the ALIGNN model. (e) Prediction of the conduction band minimum (CBM) by the ALIGNN model. (f) Prediction of the valence band maximum (VBM) by the ALIGNN model.

The screening flowchart is depicted in Fig. 2, while the process of machine learning is illustrated in Fig. 3. Initially, we screened 101036 geometrically stable perovskites out of 1569248 perovskites by applying the criteria of the tolerance factor (T_f) between 0.8 and 1.2 and octahedral factor (O_f) between 0.4 and 0.8.

Subsequently, a DFT dataset was established via computation to facilitate the further screening of stable double perovskite candidates through a stacked learning approach. To construct this dataset, 1200 double perovskites were randomly selected from the 101036 geometrically stable double perovskites for each of the two space groups, and first-principles calculations were performed on them. An ALIGNN model was trained using this dataset to filter candidates based on formation energy (E_{form}) and energy above the convex hull (E_{hull}). However, given the sensitivity of the ALIGNN algorithm to input structures, three

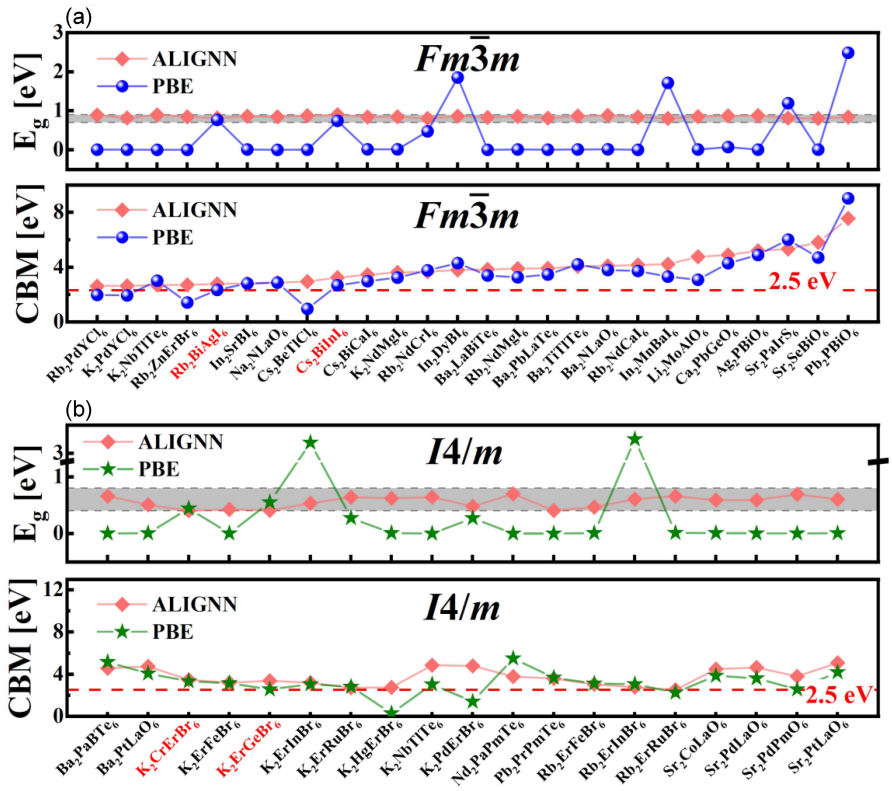

Fig. 5. (a) Predicted values of bandgap and CBM for cubic phase double perovskite that were screened out via machine learning, along with the PBE-calculated values. (b) Predicted values of bandgap and CBM for the tetragonal phase double perovskite that were screened out via machine learning, along with the PBE-calculated values.

XGBoost models were trained to predict the stable structures of candidates, thereby enhancing the precision of the screening process.

First, we used the XGBoost model to predict the lattice constants of double perovskite structures for generating the structural files for all double perovskite materials. We evaluated the performance of the model using the root mean square error (RMSE), mean absolute error (MAE), and the coefficient of determination (R^2). In this study, three XGBoost models were trained in total, one for predicting the lattice constants of the cubic phase and two for predicting the lattice constants of the tetragonal phase.

Figure 4a illustrates the performance of the XGBoost model employed for predicting the cubic phase lattice constants. Each point in this figure panel corresponds to a datum from the test set. The y axis denotes the machine learning-predicted lattice constant values, whereas the x axis represents the lattice constant values derived from the DFT-optimized structures. The model produces the following results: R^2 of 0.94, RMSE of 0.33 eV, and MAE of 0.25 eV. Figure 4b illustrates the combined performance of the two XGBoost models for predicting tetragonal phase lattice constants. Each point in this figure panel represents a data point from the test set. The machine learning-predicted lattice constant values are shown on the y axis, while the DFT-optimized lattice constant values are shown on the x axis. The model produces the following results: R^2 of 0.95, RMSE of 0.40 eV, and MAE of 0.27 eV. Values of R^2 above 90% indicate that the model performs well in the regression prediction of the lattice constant.

Later, we used the ALIGNN model to predict the energy of double perovskite materials for determining thermodynamic stability. We conducted a grid search, and the specific hyperparameter ranges are detailed in the supplementary material in Table SI [28]. Our energy predictions proved to be highly accurate for both phase structures, as indicated by R^2 close to 1. Figure 4c and d present the performance of two ALIGNN models trained to predict the structural energies of cubic and tetragonal phase materials. Each point in these figure panels corresponds to a test set data point. The machine learning-predicted structural energy values are on the y axis, and the DFT-calculated ones are on the x axis. The cubic phase model produces the following results: R^2 of 0.99, RMSE of 1.44 eV, and MAE of 1.03 eV. The tetragonal phase model, in turn, gives: R^2 of 0.99, RMSE of 1.28 eV, and MAE of 0.85 eV. We employed the data package from the Materials Project website [29] based on the Python language environment to calculate the formation

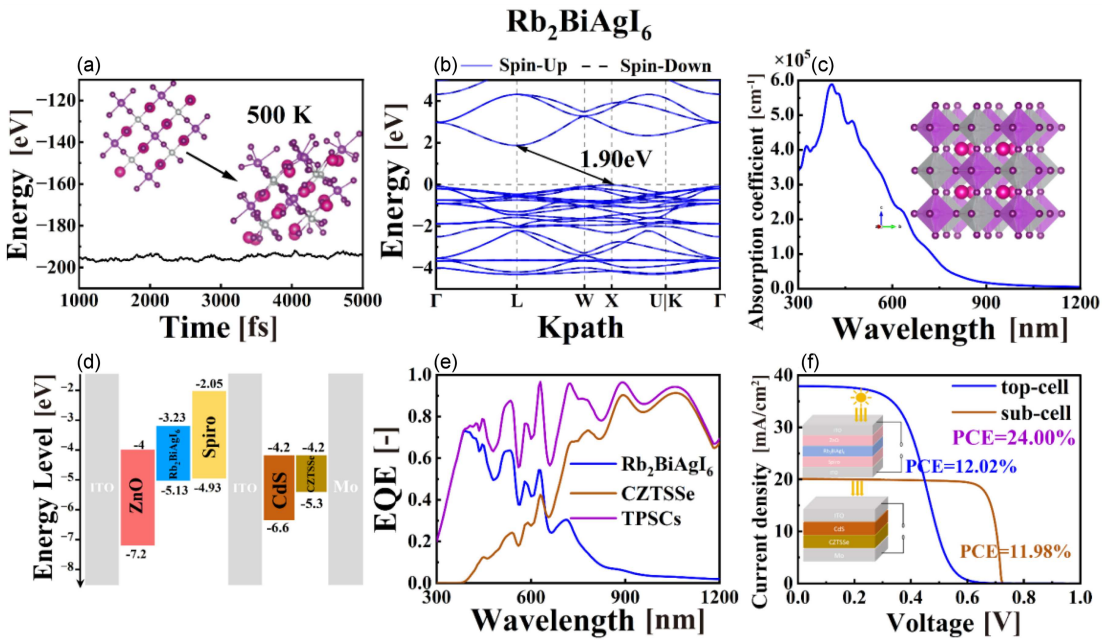

Fig. 6. DFT verification and device simulation of the cubic phase material Rb_2BiAgI_6. (a) Variations of lattice structure and energy within 5 ps at a temperature of 500 K in the AIMD simulation. (b) Band structure calculated using HSE06. (c) Calculated absorption spectra and the crystal structure. (d) Energy level diagram of different transmission layers. (e) EQE of the TPSCs device. (f) PCE and the architecture of the perovskite device.

energy (E_{form}) and the energy above the convex hull (E_{hull}) for each structure [30]. From the dataset of 101 036 cubic double perovskites and 101 036 tetragonal double perovskites, those with E_{form} and E_{hull} exceeding 0 eV/atom were excluded. Ultimately, 3812 cubic phase double perovskites and 123 tetragonal phase double perovskites were retained.

When considering the fabrication of TPSCs using perovskite materials, the materials need to undergo energy-level matching with the electron transport layer (ETL) and the hole transport layer (HTL). When CBM exceeds 2.5 eV, it can fulfill the energy-level matching requirements of common materials [31]. The bandgap is the energy disparity between CBM and VBM. Hence, the prediction of the bandgap model can also be transformed into the difference between the predictions of CBM and VBM. We used the ALIGNN models to predict CBM and VBM of double perovskite materials. Figure 4e displays the performance of the ALIGNN model for predicting CBM of both cubic and tetragonal phases. Figure 4f shows the performance of another ALIGNN model for predicting VBM of both cubic and tetragonal phases. Each point in the figure panels (e) and (f) represents a data point from the test set, with the y axis corresponding to the machine learning-predicted values and the x axis corresponding to the DFT-calculated values. The R^2 value for the CBM model is 0.91, with an RMSE of 0.54 eV and an MAE of 0.41 eV. The coefficient of determination (R^2) for the VBM model is 0.93, with an RMSE of 0.52 eV and an MAE of 0.39 eV. These indicated an excellent fit between the model's predictions and the actual CBM and VBM values of the materials.

Regarding the bandgap of perovskite materials suitable for solar cells, various literature presents different standards, and currently, there is no unified criterion. Considering the computational effects of the Perdew–Burke–Ernzerhof (PBE) functional, which tend to underestimate the bandgap, we selected materials with PBE-calculated bandgaps ranging from 0.8 to 0.9 eV for cubic phase double perovskites screening [32–34]. Due to the scarcity of tetragonal phase double perovskites, we have broadened the bandgap screening range for tetragonal phase double perovskites. The screening bandgap range of tetragonal phase double perovskite materials was 0.4 to 0.9 eV [35]. A total of 26 cubic phase double perovskites and 19 tetragonal phase double perovskites were screened out.

Finally, we verified the results from the screening through DFT calculations and ultimately determined the double perovskite materials that can be used as the top layer in TPSCs. As depicted in Fig. 5, we carried out PBE calculations for 26 cubic-phase materials and 19 tetragonal-phase materials. It was discovered that Rb_2BiAgI_6 and Cs_2BiInI_6 in the cubic phase, along with $K_2CrErBr_6$ and $K_2ErGeBr_6$ in the tetragonal phase, satisfied both the required range of the PBE bandgap and the conduction band minimum. To further investigate the properties of these four candidate materials, we utilized the HSE06 functional

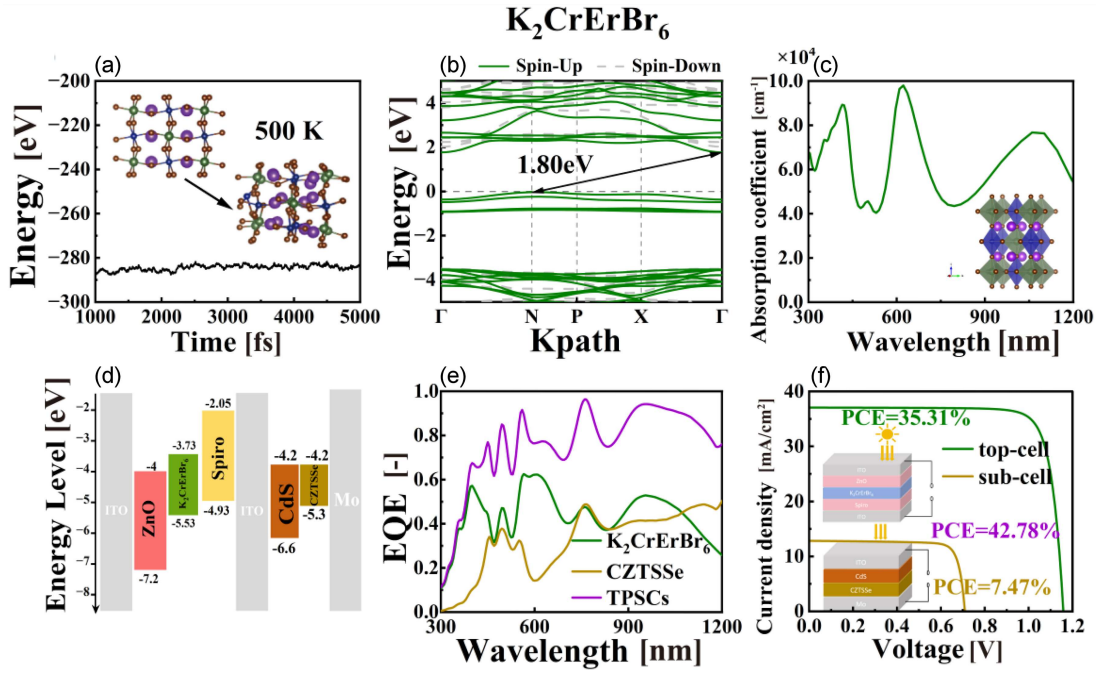

Fig. 7. DFT verification and device simulation of the cubic phase material $K_2CrErBr_6$. (a) Variations of lattice structure and energy within 5 ps at a temperature of 500 K in the AIMD simulation. (b) Band structure calculated using HSE06. (c) Calculated absorption spectra and the crystal structure. (d) Energy level diagram of different transmission layers. (e) EQE of the TPSCs device. (f) PCE and the architecture of the perovskite device.

for the calculation of the bandgaps [36, 37]. The bandgaps of Rb_2BiAgI_6, Cs_2BiInI_6, $K_2CrErBr_6$, and $K_2ErGeBr_6$ are 1.9, 1.1, 1.8, and 1.6 eV, respectively. Rb_2BiAgI_6 and $K_2CrErBr_6$ have suitable bandgaps to serve as promising absorbents for TPSCs, as illustrated in Figs. 6 and 7.

To further explore the thermal stability of the two materials, we employed *ab initio* molecular dynamics (AIMD) simulations to depict the atomic states of both materials at a high temperature of 500 K. In Fig. 6a and Fig. 7a, the 5-ps AIMD simulations of the cubic perovskite material Rb_2BiAgI_6 and the tetragonal perovskite material $K_2CrErBr_6$ at 500 K, respectively, are presented. The total energy of the two candidate materials ultimately fluctuates within a narrow range over time, suggesting that these two materials possess superior thermal stability at 500 K.

We systematically studied the optical properties of these two materials using first-principles calculations. Figures 6c and 7c show that there exists a strong absorption capacity in the solar spectral region. To more intuitively investigate the photoelectric performance of the two materials, we utilized COMSOL Multiphysics to conduct detailed simulations of tandem solar cells. As depicted in Fig. 6e, the Rb_2BiAgI_6 layer exhibits primary absorption in the range of 300 to 700 nm, while the CZTSSe layer absorbs primarily between 700 and 1200 nm. The external quantum efficiency (EQE) solar cell absorption spectrum spans from 300 to 1200 nm, achieving near-full spectrum absorption. The specific stacked materials are detailed in the illustration of Fig. 6f (the energy band diagrams can be seen in Fig. 6d). The tandem Rb_2BiAgI_6 solar cell exhibits a PCE of 24.00%. The current–voltage (J–V) characteristics of the Rb_2BiAgI_6 top-cell and the CZTSSe sub-cell are displayed in Fig. 6f. Similarly, the simulation effect of TPSCs of $K_2CrErBr_6$ is shown in Fig. 7e and f, with a PCE of 42.78%. The supporting information in Fig. S2 (see supplementary material [28]) is for the single-junction cells of Rb_2BiAgI_6 and $K_2CrErBr_6$. The relevant details of the simulation are shown in Table SII [28].

4. Conclusions

We employed machine learning to identify double perovskite materials suitable for TPSCs. Through the screening of 1569248 double perovskite materials, we identified 45 perovskite materials that exhibit thermodynamic stability and suitable bandgaps. The first-principles calculation results indicate that the cubic phase double perovskite Rb_2BiAgI_6 and the tetragonal phase double perovskite $K_2CrErBr_6$ display thermodynamic stability, suitable bandgaps, and exceptional optical absorption performance. Subsequently, we carried out further simulation studies on the photoelectric performance of these two materials. The tandem

Rb_2BiAgI_6 solar cell and the tandem $K_2CrErBr_6$ solar cell demonstrate the power conversion efficiency of 24.00% and 42.78%, respectively. Their remarkable properties are expected to play a crucial role in advancing the field of TPSCs. In general, our study presents an efficient approach for the rapid discovery and application of solar cell materials, significantly reducing the research and development cycle and making a significant contribution to the development of next-generation solar cells.

The data that support the findings of this study are available from the corresponding author upon reasonable request.

Acknowledgments

This work was supported by the National Natural Science Foundation of China (Grant Nos. 12174246, 61875119) and the Science and Technology Commission of Shanghai Municipality (Grant No. 21010501300). We would like to thank Dr. Jing Chen (Shanghai University of Electric Power) for her assistance with COMSOL simulations and Dr. Tingting Shi (Jinan University) for her support in VASP calculations.

References

[1] M. Afroz, R.K. Ratnesh, S. Srivastava, J. Singh, *Sol. Energy* **287**, 113205 (2025).

[2] N. Elumalai, M. Mahmud, D. Wang, A. Uddin, *Energies* **9**, 861 (2016).

[3] W. Shockley, H.J. Queisser, *J. Appl. Phys.* **32**, 510 (1961).

[4] S. Rühle, *Sol. Energy* **130**, 139 (2016).

[5] M. Yamaguchi, T. Takamoto, H. Juso et al., *Prog. Photovolt.* **33**, 116 (2025).

[6] J. Tong, Q. Jiang, F. Zhang, S.B. Kang, D.H. Kim, K. Zhu, *ACS Energy Lett.* **6**, 232 (2021).

[7] H. Yao, J. Zhao, Z. Li, Z. Ci, Z. Jin, *Mater. Chem. Front.* **5**, 1221 (2021).

[8] J. Wang, Y. Che, Y. Duan, Z. Liu, S. Yang, D. Xu, Z. Fang, X. Lei, Y. Li, S. (Frank) Liu, *Adv. Mater.* **35**, 2210223 (2023).

[9] G. Ji, C. Han, S. Hu, P. Fu, X. Chen, J. Guo, J. Tang, Z. Xiao, *J. Am. Chem. Soc.* **143**, 10275 (2021).

[10] X. Jiang, W.-J. Yin, *J. Energy Chem.* **57**, 351 (2021).

[11] Z. Li, Q. Xu, Q. Sun, Z. Hou, W. Yin, *Adv. Funct. Mater.* **29**, 1807280 (2019).

[12] X. Wei, Y. Zhang, X. Liu, J. Peng, S. Li, R. Che, H. Zhang, *J. Mater. Chem. A* **11**, 20193 (2023).

[13] Z. Wang, Y. Han, X. Lin, J. Cai, S. Wu, J. Li, *ACS Appl. Mater. Interfaces* **14**, 717 (2022).

[14] V.M. Goldschmidt, Die Gesetze der Krystallochemie, *Naturwissenschaften* **14**, 477 (1926).

[15] S. Burger, M.G. Ehrenreich, G. Kieslich, *J. Mater. Chem. A* **6**, 21785 (2018).

[16] Q. Sun, W.-J. Yin, *J. Am. Chem. Soc.* **139**, 14905 (2017).

[17] A.J. Howarth, T.C. Wang, S.S. Al-Juaid, S.G. Aziz, J.T. Hupp, O.K. Farha, *Dalton Trans.* **45**, 93 (2016).

[18] R. Ouyang, *Chem. Mater.* **32**, 595 (2020).

[19] G. Kresse, J. Hafner, *Phys. Rev. B* **48**, 13115 (1993).

[20] G. Kresse, J. Furthmüller, *Computat. Mater. Sci.* **6**, 15 (1996).

[21] G. Kresse, J. Furthmüller, *Phys. Rev. B* **54**, 11169 (1996).

[22] P. Borlido, J. Schmidt, A.W. Huran, F. Tran, M.A.L. Marques, S. Botti, *Npj Comput. Mater.* **6**, 96 (2020).

[23] S. Nosé, *J. Chem. Phys.* **81**, 511 (1984).

[24] W.G. Hoover, *Phys. Rev. A* **31**, 1695 (1985).

[25] V. Wang, N. Xu, J.-C. Liu, G. Tang, W.-T. Geng, *Comput. Phys. Commun.* **267**, 108033 (2021).

[26] T. Chen, C. Guestrin, in: *Proc. of the 22nd ACM SIGKDD Int. Conf. on Knowledge Discovery and Data Mining*, ACM, San Francisco 2016: p. 785.

[27] K. Choudhary, B. DeCost, *Npj Comput. Mater.* **7**, 185 (2021).

[28] Z. Wang, Z. Xiong, W. Hu, J. Jiang, Z. Cheng, Y. Xue, L. Peng, J. Lin, *Acta Phys. Pol. A* **147**, 488.s1 (2025).

[29] The Materials Project website.

[30] A. Jain, S.P. Ong, G. Hautier et al., *APL Mater.* **1**, 011002 (2013).

[31] P. Jia, M. Lu, S. Sun, Y. Gao, R. Wang, X. Zhao, G. Sun, V.L. Colvin, W.W. Yu, *Adv. Mater. Interfaces* **8**, 2100441 (2021).

[32] Z. Gao, H. Zhang, G. Mao et al., *Appl. Surf. Sci.* **568**, 150916 (2021).

[33] M.N.S. Rammoo, H.T. Abdulla, B.M. Ahmad, N.A. Abdulkareem, *PLoS ONE* **20**, e0313266 (2025).

[34] S. Adhikari, J. Clary, R. Sundararaman, C. Musgrave, D. Vigil-Fowler, C. Sutton, *Chem. Mater.* **35**, 8397 (2023).

[35] A. Talapatra, B.P. Uberuaga, C.R. Stanek, G. Pilania, *Commun. Mater.* **4**, 46 (2023).

[36] J. Heyd, G.E. Scuseria, M. Ernzerhof, *J. Chem. Phys.* **118**, 8207 (2003).

[37] A.V. Krukau, O.A. Vydrov, A.F. Izmaylov, G.E. Scuseria, *J. Chem. Phys.* **125**, 224106 (2006).